IEEE Robotics and Automation Letters (RA-L) paper, presented at ICRA 2026, Vienna, Austria. Cite as RA-L paper.

Development of a Novel 7-DOF Position-Orientation Decoupled Microsurgical Robot with Motorized Instruments for Microvascular Anastomosis

Dunfa Long, Shaoan Chen, Shuai Ao, Zhiqiang Zhang, *Senior Member, IEEE*, Chengzhi Hu, *Senior Member, IEEE*, and Chaoyang Shi, *Senior Member, IEEE*

***Abstract*—This work introduces a novel compact 7-degree-of-freedom (7-DOF) microsurgical robot with position-orientation decoupling capacity for microvascular anastomosis. The proposed system employs a modular architecture combining a proximal displacement platform for 3D small-stroke translation and a distal compact remote center of motion (RCM) mechanism for wide-range orientation adjustment. This design meets the workspace requirements for microvascular anastomosis, requiring extensive orientation adjustments with minimal positional movement and reducing the system footprint. The parasitic motion reverse self-compensation method has been developed for motorized surgical instruments, effectively reducing operational resistance to improve precision. Theoretical analysis has been performed on both the RCM mechanism and motorized surgical instruments, and kinematics-based parameter optimization and data-driven calibration have been conducted to enhance superior performance. A prototype has been constructed, and its experimental validation demonstrated that the system achieved repeatability of 11.24 $\pm$ 2.31 μm (XY) and 12.46 $\pm$ 4.48 μm (YZ), and absolute positioning accuracy of 29.80 $\pm$ 12.27 μm (XY) and 37.02 $\pm$ 19.47 μm (YZ), meeting super-microsurgical requirements. Experiments that include needle-threading and stamen peeling tasks demonstrate the robot's superior dexterity and manipulation capabilities.**

***Index Terms*—Microsurgical robot, microvascular anastomosis, RCM, position-orientation decoupling.**

I. Introduction

MICROANASTOMOSIS represents a crucial surgical procedure in microsurgery, involving intricate connections of tiny vessels, lymphatics, and nerves (0.3-3 mm in diameter) under surgical microscope magnification of 5 to 40 times [1], [2], which poses significant challenges for existing robotic surgical systems [3], [4], [5]. This procedure aims to achieve functional reconstruction in various complex surgical contexts, including lymphatic surgery, breast reconstruction, digit and limb replantation, and neurosurgery [6], [7]. Vascular anastomosis is essential for restoring blood supply and serves as a key indicator of successful reconstruction. The hand-sewn technique is the gold standard of vascular anastomosis [8], utilizing microsurgical instruments to achieve stable vessel connections, as shown in Fig. 1. Based on vessel diameter, it encompasses microsurgery (1.0-3.0 mm vessels) and super-microsurgery (0.3-1.0 mm vessels). Despite its versatility, this technique demands considerable time and expertise, particularly in super-microsurgery [9]. Currently, hand-sewn anastomosis by suturing presents multiple technical challenges. Physiological tremors and asymmetric bilateral hand coordination significantly impact surgical precision, particularly evident in super-microsurgery [9], [10], [11], [12]. The procedure requires sustained fixed postures, leading to physical fatigue, while mastering the technique demands extensive training periods. Robot-assisted microsurgery has emerged as a promising solution, utilizing robotic systems' precision for microsurgical anastomosis [13], [14], [15], primarily through the da Vinci Surgical System (Intuitive Surgical Inc., USA) and specialized robotic systems.

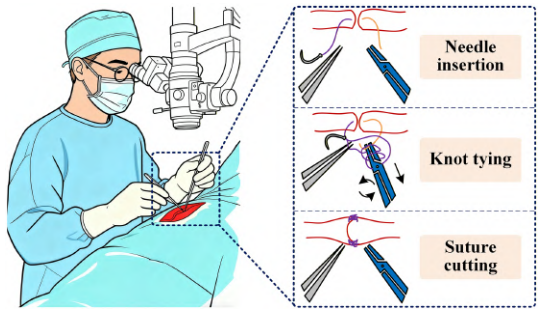

Fig. 1. Microvascular anastomosis scenarios and procedures.

The da Vinci Surgical System has been explored for its potential in microsurgical applications, with Katz et al. [16] developing a porcine free-flap model for micro-anastomosis, and Liverneaux et al. [17] conducting experiments on Wistar rat tail arteries using the da Vinci S1 system. The systems show limitations in bulky size, large instrument dimensions, and high costs in microsurgery. Several specialized microsurgical robots

Received 1 November 2025; accepted 1 December 2025. Date of publication 11 December 2025; date of current version 24 December 2025. This article was recommended for publication by Associate Editor V. Kalpathy Venkiteswaran and Editor P. Valdastri upon evaluation of the reviewers' comments. This work was supported in part by the National Natural Science Foundation of China under Grant 92148201 and Grant 52475029, and in part by the International Institute for Innovative Design and Intelligent Manufacturing of Tianjin University, Zhejiang, Shaoxing 312000, China. *(Corresponding author: Chaoyang Shi.)*

Dunfa Long, Shaoan Chen, Shuai Ao, and Chaoyang Shi are with the Key Laboratory of Mechanism Theory and Equipment Design of Ministry of Education, School of Mechanical Engineering, Tianjin University, Tianjin 300072, China (e-mail: chaoyang.shi@tju.edu.cn).

Zhiqiang Zhang is with the School of Electronic and Electrical Engineering, University of Leeds, LS2 9JT Leeds, U.K..

Chengzhi Hu is with the Department of Mechanical and Energy Engineering, Southern University of Science and Technology, Shenzhen 518055, China.

This article has supplementary downloadable material available at https://doi.org/10.1109/LRA.2025.3643333, provided by the authors.

Digital Object Identifier 10.1109/LRA.2025.3643333

IEEE Robotics and Automation Letters (RA-L) paper, presented at ICRA 2026, Vienna, Austria. Cite as RA-L paper.

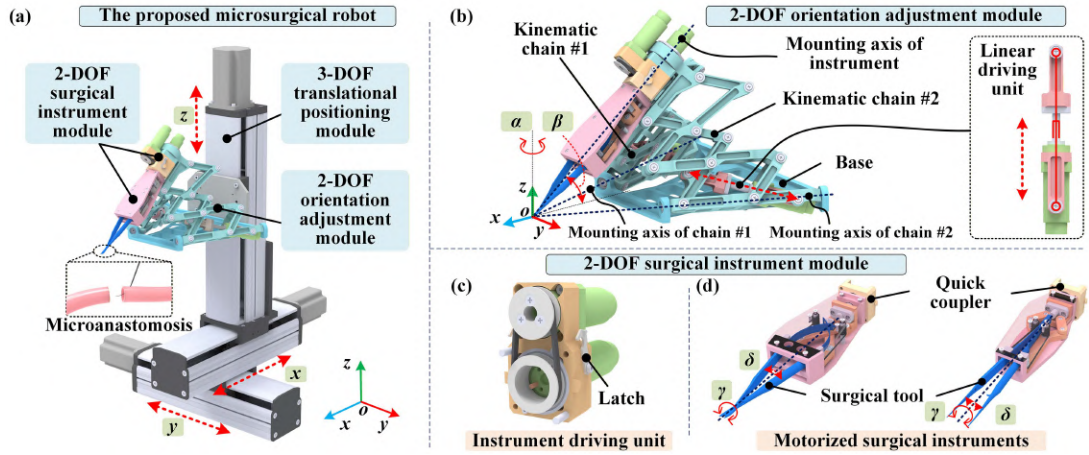

Fig. 2. The details of the proposed position-orientation decoupled microsurgical robot for microvascular anastomosis. (a) The overall design of the proposed microsurgical robot. (b) The novel parallel dual-chain RCM mechanism for the 2-DOF orientation adjustment module. (c) The instrument driving unit of the 2-DOF surgical instrument module. (d) The designed motorized surgical instruments of the 2-DOF surgical instrument module.

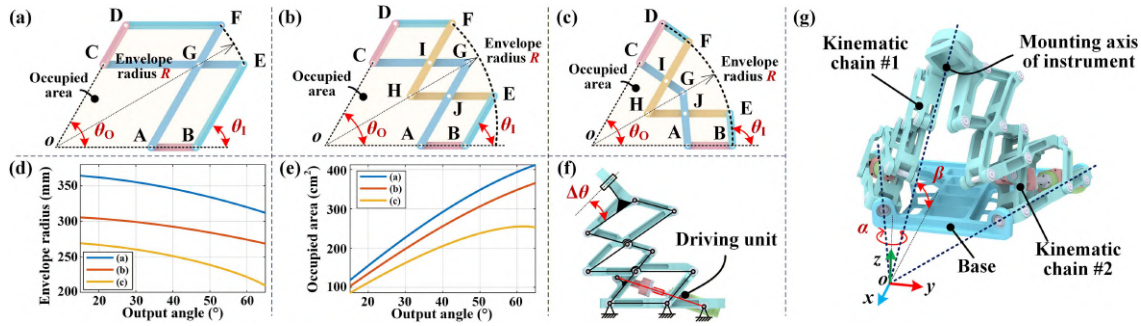

Fig. 3. Design evolution of the compact 2-DOF parallel dual-chain RCM mechanism based on improved RCM configuration. (a) Traditional dual-parallel-parallelogram RCM configuration. (b) Phase 1 of the improved RCM configuration. (c) Phase 2 of the improved RCM configuration. (d) and (e) Comparison of envelope radius R and occupied area. (f) Structural design of the improved RCM chain. (g) Final design of the compact 2-DOF parallel dual-chain RCM mechanism.

have been developed as alternatives. The Neuroarm system by Sutherland et al. [18] enables dual-arm microsurgery and single-arm stereotactic procedures, but offers insufficient accuracy (1mm) for super-microsurgery requirements. The MUSA system (Microsure Inc., NL) [19] is compatible with commercial instruments and retains the manual anastomosis operation habit. However, no report has mentioned its consideration of the parasitic motion at the instrument's tip. The Symani system (Medical Microinstruments Inc., IT) [20], equipped with 3mm microsurgical wrist instruments and 7-20X motion scaling, has advanced to clinical trials. Mitsuishi's MM-3 leader-follower system [21] features specialized surgical instruments and a position-orientation decoupled design for improved precision. However, its physical dimensions could be further reduced. Collectively, the reviewed systems highlight a persistent trade-off among footprint, dexterity, precision, and the instrument's characteristics in super-microsurgical. To overcome these issues, this work aims to develop an integrated robotic platform that combines a compact form factor, a decoupled position-orientation architecture, and inherent compensation for instrumental parasitic motions.

A compact 7-DOF position-orientation decoupled microsurgical robot has been developed for superficial micro anastomosis, featuring a modular design with a proximal small-stroke motion platform and a distal RCM mechanism. While sharing configurational similarities with ophthalmic surgical robots [4] that typically employ a 4-DOF RCM mechanism for intraocular procedures and utilize positioning modules solely for RCM mechanism placement, this system distinctively requires 7-DOF control to accommodate the complex demands of vascular anastomosis operations. The integrated surgical instrument features driving mechanisms designed based on a novel parasitic motion self-compensation method, minimizing the impact of parasitic motion at the tip. Experimental validation through prototype development and calibration demonstrates that the robot achieves high precision suitable for super-microsurgical anastomosis. Additional needle-threading and flower stamen peeling experiments further verify the robot's superior operational performance.

II. Materials and Methods

A. Requirements for Microvascular Anastomosis and Design of Position-Orientation Decoupled Follower Manipulator

According to microsurgical anastomosis procedures, precise instrument control is essential for suturing and knot-tying operations. The robotic system requires a 7-DOF configuration that includes three translational DOFs for positioning, two rotational DOFs for orientation adjustment, and two operational DOFs for the instrument's axial rotation and gripping. The workspace specifications are derived from the intrinsic characteristics of

IEEE Robotics and Automation Letters (RA-L) paper, presented at ICRA 2026, Vienna, Austria. Cite as RA-L paper.

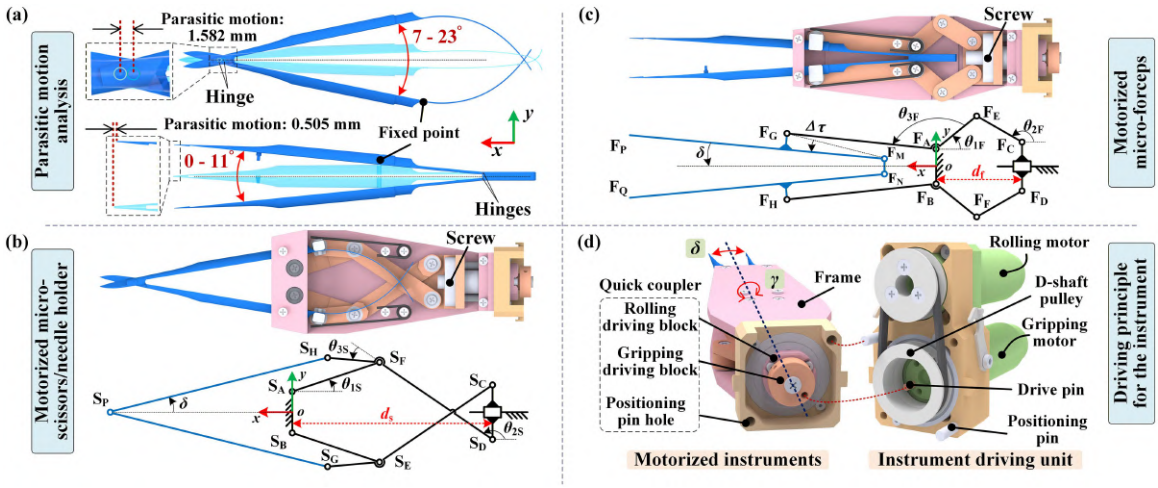

Fig. 4. Design of motorized surgical instruments. (a) Parasitic motion analysis of commercial surgical instruments. (b) Motorized micro-scissors design and its driving mechanism. (c) Motorized micro-forceps design and its driving mechanism. (d) Quick coupler and driving principle of the surgical instrument module.

microsurgical procedures. The translational workspace spans a volume of $40\times40\times50$ mm^3, covering the microscopic surgical field. The angular workspace provides a pitching range of 55° and a rolling range of ±35° to accommodate diverse instrument orientations [14], [15]. The instruments feature continuous 360° axial rotation, with gripping angles ranging from 7° to 23° for micro-scissors and from 0° to 11° for micro-forceps.

In response to these requirements, a novel 7-DOF position-orientation decoupled microsurgical robot with motorized surgical instruments has been developed for microvascular anastomosis (Fig. 2). The robot consists of three primary modules: a proximal translational positioning module using an XYZ linear platform for 3D translational movements, a distal orientation adjustment module employing a 2-DOF parallel RCM mechanism for pitching and rolling motion, and a surgical instrument module with rotation and gripping actuation, as illustrated in Fig. 2(a)). The orientation adjustment module features two kinematic chains driven by linear units, with mounting axes intersecting at the RCM point (Fig. 2(b)). The mounting axes of the kinematic chains and the instrument intersect at the RCM point. The surgical instrument module includes an instrument driving unit and two types of motorized instruments (micro-scissors/needle holder and micro-forceps), as shown in Fig. 2(c)-(d)), featuring a quick coupler interface for rapid mounting and 2-DOF actuation.

1). Design of the Parallel Dual-Chain RCM Mechanism: Given the confined microscopic space, the need for a compact design, and the need to avoid interference, the RCM mechanism was selected for the distal orientation adjustment module, enabling precise operations at the RCM point while keeping driving components away from the surgical area. A detailed analysis of the traditional dual-parallel-parallelogram configuration [22] led to an improved, more compact RCM configuration. Based on this improvement, a novel parallel dual-chain RCM mechanism was proposed, leveraging the high stiffness of parallel mechanisms for orientation adjustment.

The traditional dual-parallelogram RCM configuration in Fig. 3(a)) constrains output link CD's rotation around the RCM point via two parallelograms. Under fixed parameters including surgical operation distance OA & OC, frame/output link length AB & CD, and rotation angle θ_O, the configuration's occupied area consists of the output link motion area (sector OBD), and connecting rod occupation area (BDFE). Since sector OBD's area remains fixed due to OD's constant length, compactness improvement focused on reducing the BDFE area. Two sequential adjustments were made: first, rods DF and BE were shortened until hinge point G coincided with arc EF, as shown in Fig. 3(b)) for phase 1 improvement; then, these rods were rotated inward around hinges D and B until points E and F coincided with arc BD, resulting in the phase 2 improvement shown in Fig. 3(c)). Modeling analysis compared the traditional and improved configurations under identical parameters (OA & OC = 120mm, AB & CD = 60mm, θ_O = [15°, 70°]). As shown in Fig. 3(d)-(e)), the final improved configuration achieved 63.99% reduction in maximum envelope radius and 38.73% reduction in occupied area, showing significant compactness advantages.

Based on the final improved RCM configuration, a 2-DOF parallel dual-chain RCM mechanism was designed, considering the parallel mechanisms' high stiffness characteristics. The mechanism consists of a base and two planar RCM chains, connected via revolute joints at the base and joined for instrument mounting. The rotation amplitude was shifted upward by 8° around the RCM point for instrument installation (Fig. 3(f)). The coinciding RCM points at the intersection of chain #1, chain #2, and instrument axes form an R-RCM-R-RCM-R configuration for orientation adjustment (Fig. 3(g)).

2) Design of the 2-DOF Surgical Instruments: To improve positioning precision, a parasitic motion self-compensation method was developed to address the inherent tip displacement. Two driving mechanisms were designed for different instruments, along with an instrument driving unit providing 2-DOF actuation (Fig. 4). Commercial instruments exhibit inherent parasitic motion (Fig. 4(a)): micro-scissors and needle holders show 1.582mm X-axis parasitic displacement during 7-23° gripping motion, while micro-forceps generate 0.505mm displacement during 0-11° gripping motion.

The self-compensation method generates reverse parasitic motion at mounting points to counteract tip displacement. For micro-scissors and needle holders (Fig. 4(b)), frame rod S_AS_B and driving rod S_CS_D with ball screw sliding joint connect to the instrument via the links S_DS_H and S_CS_G. Converging hinges S_G and S_H produce reverse motion as S_CS_D moves

IEEE Robotics and Automation Letters (RA-L) paper, presented at ICRA 2026, Vienna, Austria. Cite as RA-L paper.

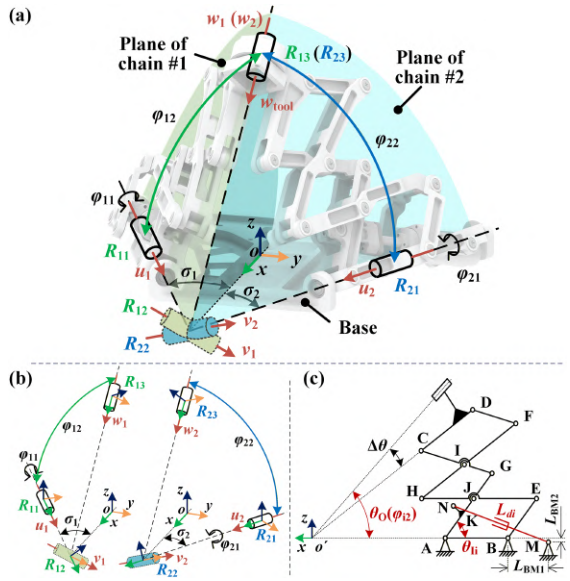

Fig. 5. (a) and (b) The simplified model and kinematic model of the proposed parallel RCM mechanism. (c) The kinematic models of the RCM chain.

along the negative x-axis, compensating motion at S_P. For micro-forceps (Fig. 4(c)), the sliding driving rod F_CF_D connects to links $F_EF_AF_G$ and $F_FF_BF_H$, with reverse motion at F_M and F_N counteracting motion at F_P and F_Q. A standardized quick coupler and instrument driving unit (Fig. 4(d)) enables instrument interchangeability and actuation. The quick coupler features positioning pin holes, a rolling driving block mounted on the frame, and a gripping driving block connecting with the screw. Instruments are mounted by aligning the positioning holes with pins. The gripping motor connects to the gripping block via a driving pin for screw rotation and grip operation, while the rolling motor drives a timing pulley with a D-shaped hole via a belt for rotary operation.

B. Kinematic Analysis of the Proposed Follower Manipulator

1) Kinematic Analysis of the Proposed RCM Mechanism: For kinematic analysis, the orientation adjustment module is simplified as a 5R mechanism (Fig. 5(a)). Each chain is modeled as a serial 3R structure, which comprises three revolute joints: the first joint (R_{i1}) connects the chain to the base; the second joint (R_{i2}), located at the RCM point, acts as an equivalent active joint with its axis normal to the chain plane; and the third joint (R_{i3}) connects the two chains at the end. The instrument shaft ($\boldsymbol{w_{tool}}$) is aligned with the axis of R_{i3}.

The base coordinate frame is defined at the RCM point; however, for illustrative clarity in Fig. 5(a)-(b)), this frame is graphically represented at the center of the base. A specific sequence of rotations determines the orientation of the $\boldsymbol{w_{tool}}$ within the base frame: initially aligned with the X-axis, the instrument is first rotated by an angle α about the base Z-axis, followed by a rotation of an angle β about the current Y-axis. The resulting X-axis direction then defines the final orientation of $\boldsymbol{w_{tool}}$. The inverse kinematics of the RCM mechanism is subsequently derived into two steps: the rotation angle φ_{i2} of the equivalent active joint R_{i2} is solved first based on the given orientation angles (α, β). Then, the actuator displacement L_{di} within the chain is calculated from the obtained φ_{i2}.

The mounting axis of the instrument and the axis vector of the simplified 5R configuration can be described as follows:

$$\begin{cases} \boldsymbol{u_i} = Rot_Z\ (\sigma_i) \cdot [1,\ 0,\ 0]^{\mathrm{T}} \\ \boldsymbol{v_i} = Rot_Z\ (\sigma_i)\, Rot_X\ (\varphi_{i1}) \cdot [0,\ 1,\ 0]^{\mathrm{T}} \\ \boldsymbol{w_i} = Rot_Z\ (\sigma_i)\, Rot_X\ (\varphi_{i1})\, Rot_Y\ (\varphi_{i2}) \\ \cdot [1,\ 0,\ 0]^{\mathrm{T}} \end{cases},\ i = 1,2 \tag{1}$$

$$\boldsymbol{w_{tool}} = Rot_Z\ (\alpha)\, Rot_Y\ (\beta) \cdot [1,\ 0,\ 0]^{\mathrm{T}} \tag{2}$$

where, $\boldsymbol{u_i}$, $\boldsymbol{v_i}$, and $\boldsymbol{w_i}$ denote the axis direction vectors of R_{i1}, R_{i2}, and R_{i3}, respectively, and $\boldsymbol{w_{tool}}$ represents the instrument axis vector in the base frame $\{O\}$, as shown in Fig. 5(a)-(b)). σ_i expresses the axis installation angle of R_{i1}, where $|\sigma_1| = |\sigma_2|$. φ_{ij} represents the joint angle of R_{ij}, where i = 12 and j = 12,3.

According to geometric relationships, vectors $\boldsymbol{w_i}$ and $\boldsymbol{w_{tool}}$ are collinear, and vector $\boldsymbol{v_i}$ is perpendicular to $\boldsymbol{w_{tool}}$. Hence, the constraint equations can be expressed as:

$$\begin{cases} \boldsymbol{w_i} \times \boldsymbol{w_{tool}} = 0 \\ \boldsymbol{v_i} \cdot \boldsymbol{w_{tool}} = 0 \end{cases},\ i = 1,2 \tag{3}$$

Combining Eq. (1) and (2) to Eq. (3), the rotation angle φ_{i2} of the equivalent active joint R_{i2} can be derived.

$$\begin{cases} \varphi_{i1} = \tan^{-1}\left(\sin\left(\alpha + \sigma_i\right) / \tan\beta\right) \\ \varphi_{i2} = \sin^{-1}\left(\sin\beta / \cos\varphi_{i1}\right) \end{cases},\ i = 1,2 \tag{4}$$

Then, based on the geometric relationships shown in Fig. 5(c)), the position of the prismatic joint L_{di} can be calculated using the output angle φ_{i2} of the RCM chain.

$$\theta_{\mathrm{Ii}} = \cos^{-1}\left(\left(L_{\mathrm{OG}}\cos\frac{\varphi_{i2}}{2} - L_{\mathrm{OA}}\right)/L_{\mathrm{AE}}\right) \tag{5}$$

$$L_{\mathrm{di}} = \sqrt{\begin{aligned}&\left[-L_{AK}\cos\theta_{\mathrm{Ii}} - L_{KN}\cos\left(\tfrac{\pi}{2} + \theta_{\mathrm{Ii}}\right) + L_{AB} + L_{BM1}\right]^2 \\ &+\left[L_{AK}\sin\theta_{\mathrm{Ii}} + L_{KN}\sin\left(\tfrac{\pi}{2} + \theta_{\mathrm{Ii}}\right) + L_{BM2}\right]^2\end{aligned}} \tag{6}$$

where, L_{BM1} and L_{BM2} denote the projected lengths of BM onto the X-axis and Z-axis, respectively.

2) Kinematic Analysis of the Proposed Surgical Instrument: The driving mechanisms for motorized micro-scissors /needle holder and micro-forceps are shown in Fig. 4(b)-(c)), both using prismatic joints as inputs to produce grip angle δ. For the micro-scissors' driving mechanism, the prismatic joint's length d_{s} varies as a function of $\theta_{1\mathrm{S}}$ and $\theta_{2\mathrm{S}}$.

$$d_{\mathrm{s}} = L_{SASF}\ \sin\theta_{1\mathrm{S}} + L_{SDSF}\sin\theta_{2\mathrm{S}} \tag{7}$$

The constraint relationships establish that S_CS_D's movement is restricted to the X direction via the prismatic joint, resulting in no Y displacement for point S_P. Moreover, point S_F's Y-coordinate can be calculated through both $\theta_{1\mathrm{S}}$ and $\theta_{2\mathrm{S}}$. These constraints facilitate the solution for $\theta_{1\mathrm{S}}$ and $\theta_{2\mathrm{S}}$.

$$\begin{cases} S_{P_y} = \frac{L_{SASB}}{2} + L_{SASF}\sin\theta_{1\mathrm{S}} + L_{SFSH}\sin\left(\theta_{2\mathrm{S}} + \theta_{3\mathrm{S}}\right) \\ \quad + L_{SHSP}\sin\delta = 0 \\ S_{Fy} = \frac{L_{SASB}}{2} + L_{SASF}\ \sin\theta_{1\mathrm{S}} = \frac{L_{SCSD}}{2} \\ \quad + L_{SDSF}\sin\theta_{2\mathrm{S}} \end{cases} \tag{8}$$

The geometric relationships yield the parasitic motion expression at instrument pivot S_P as follows:

$$\begin{aligned} S_{P_x} = L_{SASF}\ \cos\theta_{1\mathrm{S}} + L_{SFSH}\cos\left(\theta_{2\mathrm{S}} + \theta_{3\mathrm{S}}\right) \\ + L_{SHSP}\sin\delta \end{aligned} \tag{9}$$

IEEE Robotics and Automation Letters (RA-L) paper, presented at ICRA 2026, Vienna, Austria. Cite as RA-L paper.

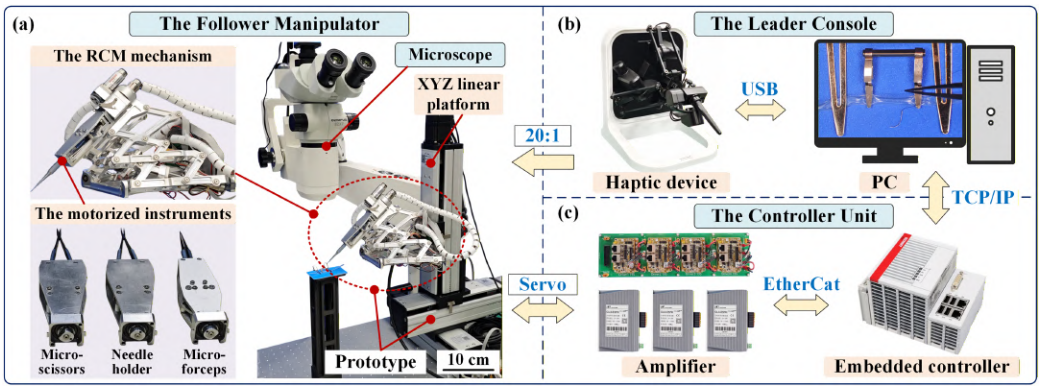

Fig. 6. The hardware configuration of the proposed microsurgical robotic system.

TABLE I
OPTIMIZATION RESULTS OF THE DESIGN OPTIMIZATION

Parameters	Optimal value	Parameters	Optimal value
σ_1/σ_2	22.5 deg	$L_{\mathrm{SASB}} \setminus L_{\mathrm{FAFB}}$	11.7 \ 10.2 mm
L_{AB}	70 mm	$L_{\mathrm{SASF}} \setminus L_{\mathrm{FAFE}}$	27.0 \ 17.0 mm
L_{BE}	50 mm	$L_{\mathrm{SFSD}} \setminus L_{\mathrm{FEFC}}$	39.8 \ 17.0 mm
L_{JH}	58 mm	$L_{\mathrm{SDSC}} \setminus L_{\mathrm{FCFD}}$	15.4 \ 13.8 mm
L_{JG}	32 mm	$\theta_{3\text{-}S} \setminus \theta_{3\text{-}F}$	28.4 \ 135 deg

Similar methods lead to the inverse kinematics solution and analytical solution for parasitic motion of the micro-forceps:

$$d_{\mathrm{f}} = L_{FAFE}\ \sin\theta_{1\mathrm{F}} + L_{FCFE}\sin\theta_{2\mathrm{F}} \tag{10}$$

$$F_{P_x} = L_{FAFG}\ \cos\left(\theta_{1\mathrm{F}} + \theta_{3\mathrm{F}}\right) - L_{FGFM}\cos\left(\delta + \Delta\tau\right) + L_{FMFP}\cos\delta \tag{11}$$

where $\Delta\tau$ donates the micro-forceps' inherent structural angle.

C. Design Optimization of the Follower Manipulator

Design optimization was performed for both the orientation adjustment and surgical instrument modules using kinematic models. For the parallel dual-chain RCM mechanism, design variables were selected as the installation angle σ_1/σ_2 between chain #1 and chain #2, along with the link lengths L_{AB}, L_{BE}, L_{JH}, and L_{JG}. The maximum envelope circle size, patient-side distance, and motion scaling factor were selected as optimization objectives, and the design was optimized using a genetic algorithm, with the results shown in Table I. Similarly, design optimization was performed on the motorized surgical instruments, with the link parameters $L_{\mathrm{SASB}}, L_{\mathrm{SASF}}, L_{\mathrm{SFSD}}, L_{\mathrm{SDSC}}, \theta_{3\_\mathrm{S}}$ (for micro-scissors), and L_{FAFB}, L_{FAFE}, L_{FEFC}, L_{FCFD}, θ_{3_F} (for micro-forceps) selected as design variables. The optimization results (also detailed in Table I) achieved significantly reduced parasitic motions of 7.7 μm and 57.8 μm for the micro-scissors and micro-forceps, respectively.

III. EXPERIMENTS AND RESULTS

A. Experimental Setup for Performance Investigation

To evaluate the performance of the proposed position-orientation decoupled microsurgical robot system, a prototype and experimental platform were developed (Fig. 6). The system operates under a leader-follower mode and consists of a surgical microscope (XT-X-5A, 8-20X, XinCheng, CN), a follower manipulator, a leader console, and a controller unit. The follower manipulator features three functional modules: a translational positioning module using an XYZ linear platform (LDRXT, CN) actuated by three stepper motors (LC57H266, Xinlichuan, CN), an orientation adjustment module with a 2-DOF RCM mechanism driven by two servo motors (DC19s, Maxon, CH), and a surgical instrument module with three interchangeable motorized end-effectors. The leader console combines a 7-DOF haptic device (CLAF-mini, Bilin Star, CN) and a PC for data processing. The controller unit includes servo amplifiers (Uservo-Flex, MotionG, CN) for orientation and instrument control, stepper amplifiers (CL3-E57H, Xinlichuan, CN) for positioning, and an embedded controller (CX-5140, Beckhoff, DE) communicating via EtherCAT bus. The workflow consists of three stages: the surgeon manipulates the haptic device under microscopic guidance; the PC processes motion data with 5-20X scaling and coordinate transformation; the controller unit receives commands via TCP/IP and executes 1000 Hz real-time servo control for precise replication.

B. Performance Investigation for the Key Modules of the Follower Manipulator

Initial investigation evaluated the orientation adjustment and surgical instrument modules, using a dual-camera unit to measure the parallel dual-chain RCM mechanism's axis deviation and tip parasitic motion.

1) The Dual-camera Measurement Unit: The dual-camera measurement unit (Fig. 7(a)) integrates orthogonally aligned cameras with backlights and manual XY platforms, achieving calibrated measurement resolutions of 2.10 μm/pixel (XZ) and 1.87 μm/pixel (YZ). The measurement methodology comprises simultaneous XZ/YZ image acquisition, followed by a comprehensive image processing sequence that includes binarization and edge detection to determine tip coordinates relative to reference positions.

2) Performance Evaluation of the RCM Mechanism: Performance evaluation of the parallel dual-chain RCM mechanism was conducted using a 1 mm-tip measurement tool at initial pose $\alpha = 0°/\beta = 40°$ (Fig. 7(a)), with tool axis distribution analysis performed through comprehensive rotational mapping across the u-axis (-35° to 35°) and the v-axis (15° to 70°) at 5° increments. The measurement unit captured images at each discrete pose, with subsequent analysis of tool axis distributions mapped in VW and UW planes (Fig. 7(b)-(c)), revealing high

IEEE Robotics and Automation Letters (RA-L) paper, presented at ICRA 2026, Vienna, Austria. Cite as RA-L paper.

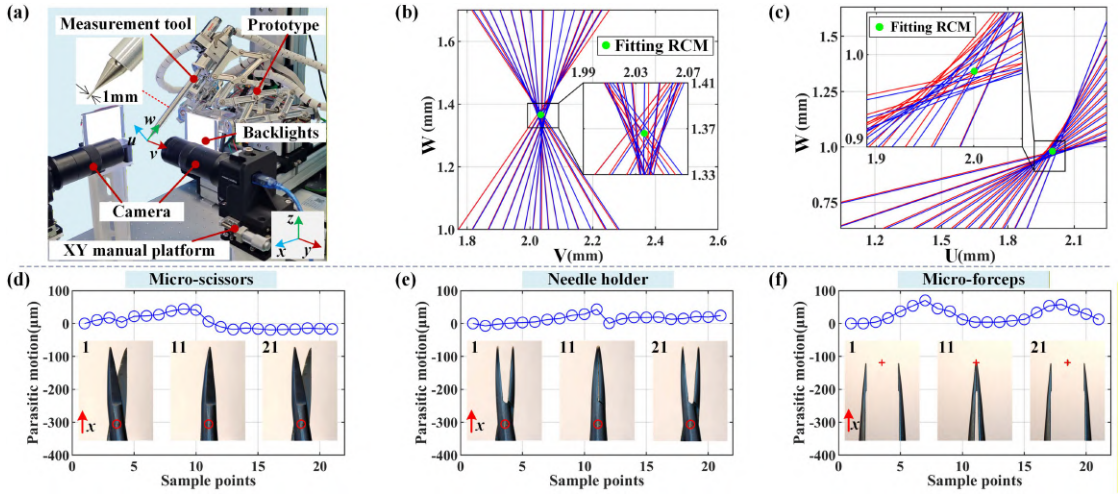

Fig. 7. (a) The setup of the utilized dual-camera measurement. (b) and (c) Instrument axis distribution during pitching and rolling motion. (d-e) The hinge's deviations of the motorized micro-scissors and the motorized needle holder. (f) The tip's deviation of the motorized micro-forceps.

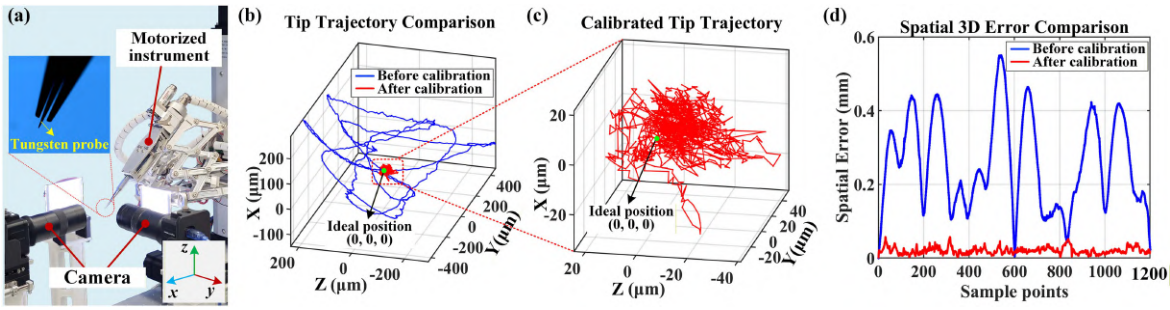

Fig. 8. Calibration of the prototyped follower manipulator. (a) The measurement setup for calibration. (b) Instrument tip deviation before and after calibration. (c) Instrument tip deviation after calibration. (d) Spatial 3D error comparison.

axis coincidence during both forward and reverse motions and convergence to a near-singular intersection point. Utilizing the midpoint of the minimal intersection region as the fitted RCM point, the mechanism demonstrated axis deviations of 15.46 ± 9.41 μm (VW plane) and 24.03 ± 14.42 μm (UW plane).

3) Performance Evaluation of the Surgical Instrument: The surgical instrument evaluation quantified x-axis deviations at micro-scissors/needle holder hinges and micro-forceps tips during open-close cycles (1.0 s closed dwell time), utilizing the measurement unit for motion recording and subsequent image processing to extract hinge axis and tip positions (Fig. 7(d)-(f)). Comprehensive analysis revealed axial deviations of 3.46 ± 22.01 μm, 13.64 ± 11.99 μm, and 25.57 ± 21.96 μm for micro-scissors, needle holders, and micro-forceps, respectively. While these measured parasitic motions exceeded theoretical calculations due to assembly tolerances and mounting misalignment, the self-compensation mechanism achieved deviations of 63.54/50.12 μm and 70.21 μm, significantly lower than the instruments' inherent parasitic motions, validating the compensation method's effectiveness.

C. Performance of the Integrated Follower Manipulator

Extensive experiments evaluated the integrated follower manipulator's performance with the designed instruments, exemplified by motorized micro-forceps.

1) Calibration for the Follower Manipulator: The calibration procedure employed a 20 μm-tip tungsten probe attached to the micro-forceps (Fig. 8(a)) to address measurement challenges posed by the 0.45 mm-wide instrument tip. The comprehensive calibration process encompassed acquiring 355 pose samples (α, β, γ) across the RCM workspace, measuring spatial coordinates (x, y, z) via measurement unit, establishing third-order polynomial relationships between input poses and output coordinates, and implementing error compensation through the XYZ linear platform. Calibration effectiveness was evaluated by maintaining the instrument tip at the coordinate origin and taking position measurements before and after calibration. Analysis of tip trajectories (Fig. 8(b)-(c)) and spatial 3D errors (Fig. 8(d)) demonstrated significant improvement, with average position deviation reduced from 259.99 ± 125.19 μm to 20.34 ± 9.26 μm.

2) Repeatability and Absolute Positioning Accuracy: Positioning performance was evaluated using a TJU-shaped path with 15 target points in XZ/YZ planes, each repeated 15 times with random RCM mechanism poses. Position distributions (Fig. 9(a),(d)) and metrics (Fig. 9(b)-(c),(e)-(f)) showed highly concentrated positional clustering around intended targets. The system achieved repeatability and absolute positioning accuracy of 11.24 ± 2.31 μm and 29.8 ± 12.27 μm in the XZ plane, and 12.46 ± 4.48 μm and 37.02 ± 19.47 μm in the YZ plane, meeting microsurgical requirements.

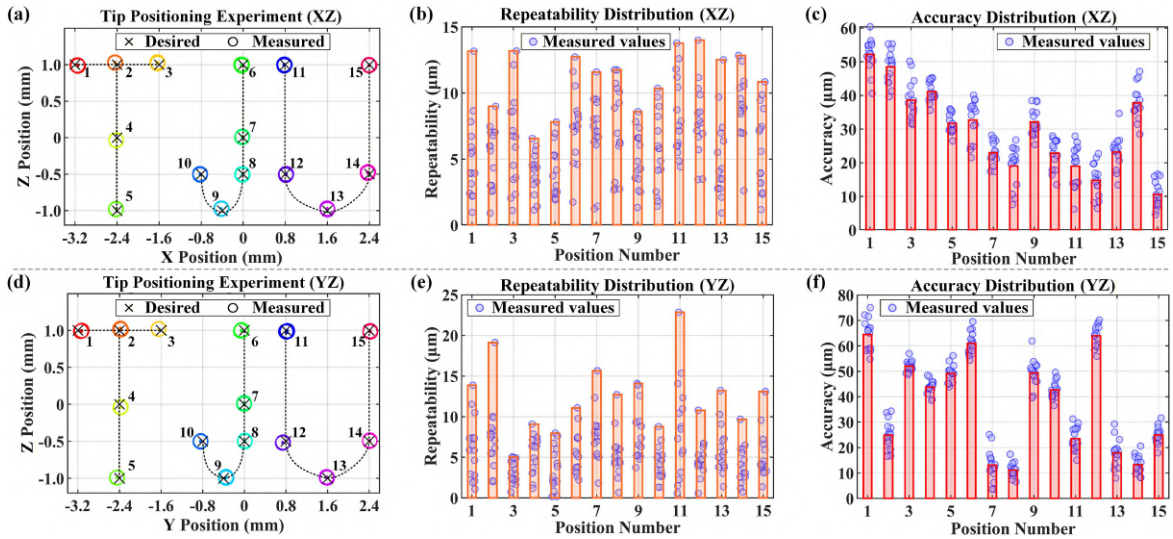

Fig. 9. Tip positioning experiment results in XZ and YZ planes. (a) and (d) The desired points and the distribution of the measured points in the XZ and YZ planes. (b) and (c) Repeatability and accuracy distribution in the XZ plane. (e) and (f) Repeatability and accuracy distribution in the YZ plane.

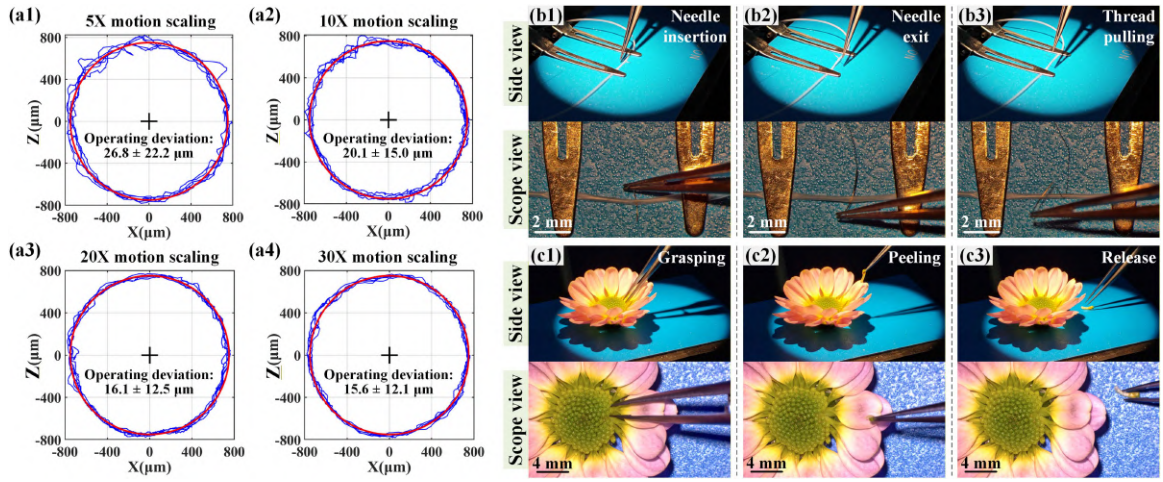

Fig. 10. (a) Instrument tip trajectory under 5- 30X motion scale in leader-follower mode. (b) Suturing task operations: (b1) Needle insertion. (b2) Needle exit. (b3) Thread pulling. (c) Stamen peeling task operations: (c1) Grasping. (c2) Peeling. (c3) Release.

3) Operational Accuracy in the Leader-Follower Mode: Leader-follower performance testing across motion scaling factors (5X-30X) using measurement unit (Fig. 10(a)) showed operational accuracies of 26.8 ± 22.2 μm (5X), 20.1 ± 15.0 μm (10X), 16.1 ± 12.5 μm (20X), and 15.6 ± 12.1 μm (30X). While notable precision improvements of 40% were observed from 5X to 20X scaling, only a minimal improvement (3%) occurred between 20X and 30X, likely attributable to reaching the inherent precision limitations of the selected haptic device. Nevertheless, the system achieved operational accuracies meeting microsurgical requirements across all scaling factors.

4) Operation for Simulation Tasks: Validation tasks performed by an operator without any medical background included suture insertions into 0.5mm simulated vessels (Fig. 10(b)) and 0.5mm daisy stamen manipulation (Fig. 10(c)). The operator completed two suturing operations in 113 and 119 seconds, while four stamen peeling procedures averaged 77 seconds. Extended operation times were attributed to single-manipulator limitations, specifically the absence of a second arm for vessel stabilization. Future development will incorporate an additional robotic arm to enable bilateral operations.

D. Discussion

Table II compares the proposed robotic system with existing robotic systems in configuration, preserving the surgeon's operating habits, repeatability, absolute positioning accuracy, and leader-follower operation accuracy. The proposed microsurgical robot utilizes a position-orientation decoupled design (proximal: XYZ; distal: RCM), demonstrating the potential for a compact structure if a commercial large-sized three-axis platform is replaced. Hence, future development will focus on a compact 3T mechanism to further enhance system compactness. This robotic system's instrument is modified based on the commercial instruments, preserving the surgeon's operating habits, while the parasitic motion self-compensation method improves operational accuracy compared to the MUSA system. The robot

TABLE II
COMPARISONS WITH STATE-OF-THE-ART WORKS

System	Configuration	Preserving the surgeon's operating habits	Repeatability	Absolute positioning accuracy	Leader-follower operation accuracy
da Vinci	Position-orientation coupling	No	NG	NG	<1000 μm
MUSA	Position-orientation coupling	Yes	15 μm	70 μm	30-40 μm
Symani	Position-orientation coupling	No	NG	NG	NG
MM-3	Position-orientation decoupled (proximal: RCM, distal: XYZ)	No	NG	NG	44 μm
ASTEM A	Position-orientation decoupled (proximal: XYZ, distal: RCM)	No	9-14 μm	58 μm	9-22 μm
This work	Position-orientation decoupled (proximal: XYZ, distal: RCM)	Yes (with PM compensated)	11.24±2.31 μm (XZ) 12.46±4.48 μm (YZ)	29.80±12.27 μm (XZ) 37.02±19.47 μm (YZ)	16.1±12.5 μm (20X) (without tremor suppression)

NG: not given or not found in the current materials; PM: parasitic motion

demonstrates repeatability of 11.24 ± 2.31 μm (XZ) and 12.46 ± 4.48 μm (YZ), absolute positioning accuracy of 29.8 ± 12.27 μm (XZ) and 37.02 ± 19.47 μm (YZ), and leader-follower operation accuracy of 16.1 ± 12.5 μm at 20X magnification without tremor suppression. These precision metrics either surpass or match those of state-of-the-art systems, fulfilling microsurgical requirements. Future work will focus on implementing a compact 3T mechanism, building a dual-arm robot system that integrates a passive robotic arm and two 7-DOF robotic arms, developing adaptive tremor suppression algorithms for model and ex vivo experiments, and investigating the potential for deep microsurgery applications.

IV. CONCLUSION

This letter presents a novel 7-DOF position-orientation decoupled microsurgical robot for superficial microvascular anastomosis, featuring a proximal small-stroke translational platform, a distal compact RCM mechanism, and motorized surgical instruments with parasitic motion self-compensation. The system achieves structural compactness through kinematic matching of surgical demands, minimizing operating room space occupation. Experimental evaluation demonstrated super-microsurgical precision, validated through needle threading and flower stamen peeling tasks. The improved RCM configuration provides insights for developing compact surgical robots, while the parasitic motion self-compensation method offers a novel solution for undesired motion. Future work will address dual-arm cooperation, FBG-based force-shape sensing [23], [24], and visual navigation.

REFERENCES

[1] S. Lohasammakul, S. J. Lee, C. Suppasilp, N. Sirivongs, K. Koedpuech, and T. Numwong et al., "A clinical application for arterial coupling and histomorphometric comparison of internal mammary and thoracodorsal arteries for safe use," *Microsurgery*, vol. 44, 2024, Art. no. e31214.

[2] A. Syed Ahmed, T. Akina, E. T. Jason, L. Shawn, F. Nicole, and L. Pierre et al., "Technological advancements in head and neck free tissue transfer reconstruction," *Plast. Aesthetic Res.*, vol. 8, 2021, Art. no. 35.

[3] Y. Hu, W. Li, L. Zhang, and G.-Z. Yang, "Designing, prototyping, and testing a flexible suturing robot for transanal endoscopic microsurgery," *IEEE Robot. Automat. Lett.*, vol. 4, no. 2, pp. 1669–1675, Apr. 2019.

[4] N. Wang, X. Zhang, M. Li, H. Zhang, D. Stoyanov, and A. Stilli, "A 5-DOFs robot for posterior segment eye microsurgery," *IEEE Robot. Automat. Lett.*, vol. 7, no. 4, pp. 10128–10135, Oct. 2022.

[5] Y. Liu, D. Song, G. Zhang, Q. Bu, Y. Dong, and C. Hu et al., "A novel electromagnetic driving system for 5-DOF manipulation in intraocular microsurgery," *Cyborg Bionic Syst.*, vol. 5, 2024, Art. no. 0083.

[6] M. M. Jonczyk, J. Jean, R. Graham, and A. Chatterjee, "Surgical trends in breast cancer: A rise in novel operative treatment options over a 12 year analysis," *Breast Cancer Res. Treat.*, vol. 173, pp. 267–274, 2019.

[7] N. Lindenblatt, L. Grünherz, A. Wang, E. Gousopoulos, C. Barbon, and S. Uyulmaz et al., "Early experience using a new robotic microsurgical system for lymphatic surgery," *Plast. Reconstructive Surg.*, vol. 10, 2022, Art. no. e4013.

[8] M. Wang, H. Guo, G. Zhang, P. Ruan, and K. Zhi, "Development and innovation of modern microvascular anastomoses," *J. Biosciences Medicines*, vol. 12, pp. 105–118, 2024.

[9] T. Wang, H. Li, T. Pu, and L. Yang, "Microsurgery Robots: Applications, design, and development," *Sensors Basel*, vol. 23, 2023.

[10] M. M. Aitzetmüller, M.-L. Klietz, A. F. Dermietzel, T. Hirsch, and M. Kückelhaus, "Robotic-assisted microsurgery and its future in plastic surgery," *J. Clin. Med.*, vol. 11, 2022, Art. no. 3378.

[11] C. Bergeles and G.-Z. Yang, "From passive tool holders to microsurgeons: Safer, smaller, smarter surgical robots," *IEEE Trans. Biomed. Eng.*, vol. 61, no. 5, pp. 1565–1576, May 2014.

[12] I. Carlotta, G. Lisanne, and L. Nicole, "Systematic review of robotic-assisted peripheral and Central lymphatic surgery," *J Surg. Oncol.*, 2024.

[13] M. M. Marinho, K. Harada, K. Deie, T. Ishimaru, and M. Mitsuishi, "SmartArm: Suturing feasibility of a surgical robotic system on a neonatal chest model," *IEEE Trans. Med. Robot. Bionics*, vol. 3, no. 1, pp. 253–256, Feb. 2021.

[14] L. Vanthournhout, J. Szewczyk, J. Duisit, B. Lengelé, B. Raucent, and B. Herman, "ASTEMA: Design and preliminary performance assessment of a novel tele-microsurgery system," *Mechatronics*, vol. 81, 2022, Art. no. 102689.

[15] U. J. Yang, D. Kim, M. Hwang, D. Kong, J. Kim, and Y. H. Nho et al., "A novel microsurgery robot mechanism with mechanical motion scalability for intraocular and reconstructive surgery," *Int. J. Med. Robot. Comput. Assist. Surg.*, vol. 17, 2021, Art. no. e2240.

[16] R. D. Katz, G. D. Rosson, J. A. Taylor, and N. K. Singh, "Robotics in microsurgery: Use of a surgical robot to perform a free flap in a pig," *Microsurgery*, vol. 25, pp. 566–569, 2005.

[17] P. A. Liverneaux, S. Hendriks, J. C. Selber, and S. J. Parekattil, "Robotically assisted microsurgery: Development of basic skills course," *Arch. Plast. Surg.*, vol. 40, pp. 320–326, 2013.

[18] G. R. Sutherland, P. B. McBeth, and D. F. Louw, "NeuroArm: An MR compatible robot for microsurgery," *Int. Congr. Ser.*, vol. 1256, pp. 504–508, 2003.

[19] F. O. F. Reilly, A. Nilsson, H. Frieberg, M. S. Mayr-Riedler, and M. Mani, "Implementation of robot-assisted lymphaticovenous anastomoses in a microsurgical unit," *Eur. J. Plast. Surg.*, vol. 47, 2024.

[20] S. Gorji, K. Wessel, A. Dermietzel, M. Aitzetmueller, I. Wendenburg, and C. Varnava et al., "Fully telemetric robotic microsurgery: Clinical experience with 23 cases," *Microsurgery*, vol. 44, 2024, Art. no. e31227.

[21] M. Mitsuishi, A. Morita, N. Sugita, S. Sora, R. Mochizuki, and K. Tanimoto et al., "Master–Slave robotic platform and its feasibility study for micro-neurosurgery," *Int. J. Med. Robot. Comput. Assist. Surg.*, vol. 9, pp. 180–189, 2013.

[22] C.-H. Kuo, J. S. Dai, and P. Dasgupta, "Kinematic design considerations for minimally invasive surgical robots: An overview," *Int. J. Med. Robot. Comput. Assist. Surg.*, vol. 8, pp. 127–145, 2012.

[23] J. Hao, Z. Zhang, S. Wang, and C. Shi, "2D Shape estimation of a pneumatic-driven soft finger with a large bending angle based on learning from two sensing modalities," *Adv. Intell. Syst.*, vol. 5, no. 10, 2023, Art. no. 2200324.

[24] Y. Lu, B. Lu, B. Li, H. Guo, and Y.-H. Liu, "Robust three-dimensional shape sensing for flexible endoscopic surgery using multi-core FBG sensors," *IEEE Robot. Automat. Lett.*, vol. 6, no. 3, pp. 4835–4842, Jul. 2021.